

Systematic bias in baroclinic energy estimates in shelf seas

Stephenson, Gordon; Green, Mattias; Inall, Mark E.

Journal of Physical Oceanography

Published: 01/09/2016

Peer reviewed version

[Cyswllt i'r cyhoeddiad / Link to publication](#)

Dyfyniad o'r fersiwn a gyhoeddwyd / Citation for published version (APA):

Stephenson, G., Green, M., & Inall, M. E. (2016). Systematic bias in baroclinic energy estimates in shelf seas. *Journal of Physical Oceanography*, 46(9).

Hawliau Cyffredinol / General rights

Copyright and moral rights for the publications made accessible in the public portal are retained by the authors and/or other copyright owners and it is a condition of accessing publications that users recognise and abide by the legal requirements associated with these rights.

- Users may download and print one copy of any publication from the public portal for the purpose of private study or research.
- You may not further distribute the material or use it for any profit-making activity or commercial gain
- You may freely distribute the URL identifying the publication in the public portal ?

Take down policy

If you believe that this document breaches copyright please contact us providing details, and we will remove access to the work immediately and investigate your claim.

Systematic bias in baroclinic energy estimates in shelf seas

Gordon R. Stephenson* and J. A. Mattias Green[†] and Mark E. Inall[‡]

*Bangor University, School of Ocean Science, Askew St., Menai Bridge, Isle of Anglesey, LL59

5AB, UK

[†]*Corresponding author address:* Bangor University, School of Ocean Science, Askew St., Menai

Bridge, Isle of Anglesey, LL59 5AB, UK

E-mail: m.green@bangor.ac.uk

[‡]Scottish Association for Marine Science, Scottish Marine Institute, Oban, Argyll, PA37 1QA, UK

ABSTRACT

9 A simple model of an internal wave advected by oscillating barotropic flow
10 suggests flaws in standard approaches to estimating properties of the internal
11 tide. When the M_2 barotropic tidal current amplitude is of similar size to
12 the phase speed of the M_2 baroclinic tide, spectral and harmonic analysis
13 techniques lead to erroneous estimates of the amplitude, phase, and energy in
14 the M_2 internal tide. In general, harmonic fits and bandpass or low-pass filters
15 that attempt to isolate the lowest M_2 harmonic significantly underestimate
16 the strength of M_2 baroclinic energy fluxes in shelf seas. Baroclinic energy
17 flux estimates may show artificial spatial variability, giving the illusion of
18 sources and sinks of energy where none are present. Analysis of previously
19 published estimates of baroclinic energy fluxes in the Celtic Sea suggests this
20 mechanism may lead some values to be 25 to 60% too low.

21 **1. Introduction**

22 Interactions of the barotropic tide with sloping ocean bathymetry in the presence of stratification
23 produce tidal-frequency internal waves, the internal tide, that carry energy to the ocean interior or
24 to the continental margins (see, e.g., Wunsch and Ferrari, 2004 for a review). Where these internal
25 waves break, the result is turbulence, energy dissipation and, potentially, vertical mixing. Internal
26 waves are consequently the main source of dissipation in the abyssal ocean (e.g., Wunsch and
27 Ferrari, 2004), but a significant fraction of the tidal energy in shelf seas is in the internal wave
28 field, with the mode-1 semidiurnal (M_2) tide responsible for an estimated 20-60 GW of energy
29 propagating shoreward of the 175 m isobath and another 40-120 GW dissipating on the continental
30 shelf slope (Kelly et al., 2013). Ocean circulation patterns are sensitive to the global distribution of
31 the resulting vertical mixing (Melet et al., 2013). Locally, breaking internal waves cause vertical
32 mixing that enhances vertical nutrient transport (Sharples et al., 2001) and contributes to the high
33 primary productivity of the shelf break region, indirectly supporting fisheries (Sharples et al.,
34 2007). Internal tides can create strong vertical shear in the water column, which can impact drilling
35 and dredging operations (Osborne et al., 1978), as well as tidal power generation schemes.

36 Observations of the internal tide in shelf seas reveal many poorly explained features of the
37 wave field. Spectra often show considerable energy at higher harmonics of the semidiurnal (M_2)
38 tide (Rippeth and Inall, 2002; Robins and Elliott, 2009; Shroyer et al., 2011). In some cases,
39 higher harmonics may be more evident than the fundamental tide or inertial forcing frequency,
40 as shown for higher vertical modes by MacKinnon and Gregg (2003). Furthermore, large spatial
41 and temporal variability in the strength and phase of the internal tide is common: off the coast
42 of New Jersey, Shroyer et al. (2011) observed spatial variability in baroclinic energy fluxes, with
43 both increases and decreases in strength moving from continental slope to shelf. These energy

44 fluxes were also concentrated in one or two “pulses” during particular phases of the barotropic
45 tide. This intermittency is often associated with nonlinear internal waves (NLIW). However, as
46 we demonstrate in this article, a linear superposition of barotropic and baroclinic waves can lead
47 to many of the features often associated with NLIW.

48 Although the generation mechanisms of the internal tide are fairly well understood and the
49 energy conversion rate can be quantified (Green and Nycander, 2013), internal tides have proven
50 difficult to predict, and temporal variability in the internal tide has been hard to explain. Nash et al.
51 (2012) hypothesized that the locally-generated component of the internal tide should have a fixed
52 phase relationship to the local barotropic tide, but that long-distance propagation of the internal
53 tide across ocean basins, through mesoscale variability, results in remotely-generated internal tides
54 with an incoherent phase relationship to the local barotropic tide. Nash et al. (2012) decomposed
55 the internal tide into coherent, locally-generated and incoherent, remotely-generated components,
56 and found that the majority of shoreward propagating energy has a time-varying phase offset rel-
57 ative to the local barotropic tide. They therefore concluded that the internal tide on the New
58 England continental shelf is mostly generated at remote locations. Further results incongruous
59 with local barotropic forcing were seen by Hopkins et al. (2014) and Inall et al. (2000), who saw
60 that baroclinic energy fluxes on the European shelf decreased in strength during the spring tide,
61 when generating forces should be greatest. The distribution of energy over vertical wave modes is
62 also often a mystery; MacKinnon and Gregg (2003) found that the distribution of energy between
63 different vertical modes of the M_2 tide varies in time, but with no apparent pattern or coherence.

64 While the many processes contributing to temporal and spatial variability in the internal tide
65 make internal tide prediction a complicated task, there remains considerable uncertainty in more
66 elementary properties of the wave field. In the Celtic Sea, values of the average onshore baroclinic
67 energy flux, an important sink term in the global tidal energy budget, range from 73 W m^{-1} (Green

et al., 2008) or 100 W m^{-1} (Hopkins et al., 2014) to as much as 1600 W m^{-1} (Inall et al., 2011), a difference of more than an order of magnitude. In the Celtic Sea, some of the variability in baroclinic energy fluxes has been attributed to the complicated nature of bathymetry at the shelf (Vlasenko et al., 2014) or to changes in propagation across the shelf (Stephenson et al., 2015). Some part of the difference may be due to the positioning of moorings, time of year, or analysis techniques used. Understanding the cause of such a wide spread in observed energy fluxes, and whether the same processes apply to other shelf seas, is vital to understanding global patterns of tidal energy loss and vertical mixing.

The objective of this paper is to examine the implications of barotropic / baroclinic tide interactions for baroclinic energy flux estimates. We show that some of the temporal and spatial variability of the internal tide can be explained by a fairly simple advective process. This wave advection process is a very simple case of the wave-wave interactions examined by Holloway (1983) and Pinkel (2008). Those studies sought to reconstruct the internal wave wavenumber-frequency spectral continuum observed in the open ocean by modeling the effects of wave-wave advection and Doppler "smearing" by oceanic currents on the spectra of an internal wave field constructed of waves of discrete frequencies. In this paper, we consider only interactions between the barotropic tide and one mode of the baroclinic tide; we are interested in the consequences this interaction has on estimates of the strength of the baroclinic tide and energy fluxes. Following Green et al. (2010), we model a sinusoidal internal tide advected by a sinusoidally oscillating barotropic tidal flow. With this linear superposition of a mode-0 and mode- n wave, we reproduce many of the features of the internal tide described above. Furthermore, we find that, where the barotropic tide is strong, standard analysis techniques and filters may lead to significant underestimates of the strength of the internal tide and of baroclinic energy fluxes.

91 Section 2 describes our model of an advected internal wave. Section 3 discusses the features
 92 of the model advected wave, while the implications for shelf-seas observations of the tide are
 93 discussed in Section 4. Conclusions are in Section 5.

94 2. Methods

95 We assume that a sinusoidal plane wave of a single frequency propagates at an angle θ measured
 96 clockwise from north. This wave can represent many things: the displacement of the thermocline
 97 in a two-layer wave, or the baroclinic velocity at a fixed depth, or anything that is in the form of a
 98 linear, sinusoidal wave, and we thus write:

$$\eta(x, y, t) = A \sin(k \sin(\theta)x + k \cos(\theta)y - \omega t) + B, \quad (1)$$

99 where A is the wave amplitude (of, e.g. isopycnal displacement or baroclinic velocity), B is the
 100 mean value, k is the horizontal wavenumber, and ω is the frequency of the wave, in the following
 101 assumed to be that of the M_2 tide, $2\pi/12.42 \text{ hour}^{-1}$. The phase velocity of the internal wave is
 102 defined as $c = \omega/k$.

103 We assume that the internal wave remains sinusoidal when viewed from a reference frame mov-
 104 ing with the advective flow. To represent the advection of the propagating wave by the barotropic
 105 flow, we replace x and y by $x_{adv}(t)$ and $y = y_{adv}(t)$, where

$$x_{adv}(t) = x - \int_{t_0}^t U_{bt}(\tau) d\tau \quad \text{and} \quad y_{adv}(t) = y - \int_{t_0}^t V_{bt}(\tau) d\tau \quad (2)$$

106 account for advection of the internal wave by barotropic flow U_{bt} in the east-west direction and
 107 V_{bt} in the north-south direction. We introduce

$$x_r = \sin(\theta) x + \cos(\theta) y \quad \text{and} \quad U_{rot} = \sin(\theta) U_{bt} + \cos(\theta) V_{bt} \quad (3)$$

to represent the coordinates and advective motions projected into the direction of propagation of the wave. In these new coordinates, the expression for the advected wave is simplified to

$$\eta(x_r, t) = A \sin \left(k \left(x_r - \int_{t_0}^t U_r(\tau) d\tau \right) - \omega t \right) + B. \quad (4)$$

In a coordinate system moving with the component of barotropic flow in the direction of wave propagation, say x^* , where

$$x^*(x_r, t) = x_r - \int_{t_0}^t U_r(\tau) d\tau = \sin(\theta) x_{adv} + \cos(\theta) y_{adv}, \quad (5)$$

the equation has the familiar form

$$\eta(x^*, t) = A \sin(kx^* - \omega t) + B. \quad (6)$$

In the transition to a stationary coordinate system, as at a mooring where x and y are fixed, the observed wave has a different expression as a function of time. For a semidiurnal tide, the barotropic tidal velocity is represented as $U_r = U \cos(\omega t)$, where U is amplitude of the tide projected into the wave propagation direction. The waveform observed at a fixed (Eulerian) point in space, η_0 , can be expressed as

$$\eta_0(t) = A \sin \left(\frac{U}{c} \sin(\omega t) - \omega t + \Phi_0 \right) + B. \quad (7)$$

The observed waveform is strongly dependent on the barotropic/baroclinic phase difference Φ_0 , which is a function of x_r (distance along the direction of wave propagation). Therefore, the observed wave and its energy and spectral characteristics also vary in x_r . The phase offset between the barotropic tide and the mode- n baroclinic tide can be written

$$\Phi_0 = (k_n - k_0)x_r, \quad (8)$$

where k_n is the horizontal wavenumber of the mode- n internal tide and k_0 is the horizontal wavenumber of the barotropic tide. k_0 is generally much smaller than k_n , so $\Phi_0 \approx k_n x_r$. A π

125 radian difference in Φ_0 corresponds to $\sim \frac{1}{2}\lambda_n$, where λ_n is the horizontal wavelength of the n^{th} -
 126 mode internal tide.

127 The physics at work are similar in nature to a Doppler shift; the observed frequency changes as a
 128 result of the wave moving relative to the observer. The key difference is that the frequency of mo-
 129 tion is close to that of the wave being observed. In a standard Doppler shift, $\omega_{shifted} = \omega_{true} \pm Uk$,
 130 but this formulation is insufficient to describe the observed waveform when the wave and advective flow have similar frequencies. As we shall see, in this case, the frequency shift occurs in
 131 discrete steps – to multiples (harmonics) of ω . If there is no barotropic flow (i.e., if $U = 0$), our
 132 case reduces to that of a purely sinusoidal wave with all its energy at the M_2 frequency. Because
 133 the barotropic flow is vertically uniform and purely horizontal, we can describe a baroclinic tide
 134 propagating in the vertical and horizontal directions as a set of stacked horizontally propagating
 135 waves, each at a phase offset from the one above. As it is advected, under our simplifying assumptions,
 136 the tidal beam retains its shape, and the effects on each layer can be computed independently
 137 using the appropriate phase as a function of depth. For the same reason, vertically well-resolved
 138 measurements will not mediate the effects of the barotropic advection on the observed waveforms.
 139

140 3. Results

141 *a. Waveforms*

142 Although the model wave is sinusoidal in x^* and t (Equation 2), Eulerian measurements of the
 143 wave (represented by η_0 in Equation 2) are not sinusoidal (Figure 1). Two parameters govern
 144 the observed waveform; Φ_0 , the phase offset between the baroclinic and barotropic wave; and
 145 U/c , the amplitude of the barotropic flow normalized by the internal wave speed. The observed
 146 waveform retains its 12.42 hour periodicity, but exhibits several unusual features that vary with

147 the normalized barotropic flow speed, U/c , as well as the phase offset between the baroclinic and
 148 barotropic flows, Φ_0 . At small values of U/c , these features are limited to a steepening of the
 149 wave crest. At larger values of U/c , the observed waveform appears more nonlinear, whereas
 150 multiple wave crests advected past the observing platform during one tidal period appear as higher
 151 frequency signals. Other shapes are possible: at certain phase-offsets, the waves in Figure 1 look
 152 like low-frequency solitons (see, e.g., Figure 1b,f). In this example, $U/c \approx 2$, and the trough
 153 or crest is evident for only about 3 hours. One of these waves appears as a wave of elevation
 154 (Figure 1f); the other, at a phase offset π radians different from the first, is a wave of depression
 155 (Figure 1c).

156 The criteria that U/c be large is equivalent to the flow having a large tidal excursion length scale.
 157 With a large tidal excursion, many crests and troughs may be advected past a fixed observer. An
 158 important note, though, is that this ratio is a property of the internal wave being considered. Higher
 159 vertical modes are slower and have shorter horizontal wavelengths than lower vertical modes. In
 160 uniform stratification, for example, the phase speed of the n^{th} vertical mode, c_n , scales inversely
 161 with mode number n , therefore U/c_n scales linearly in n . Higher vertical mode waves therefore
 162 are likely to exhibit a greater degree of distortion as a result of advection.

163 *b. Average values*

164 Waves are often identified as perturbations to the mean state of some property of the ocean. For
 165 example, if $h(t)$ represents the depth of the thermocline, $h(t)$ might be decomposed into $h(t) =$
 166 $\overline{h(t)} + h'(t)$, where h' is the perturbation associated with a wave and the overbar indicates averaging
 167 over some integer number of wave periods. For a linear internal wave, $\overline{h'} = 0$. When $U/c > 0$,
 168 however, the time-average of wave properties observed at a fixed location may be non-zero (as in
 169 Figure 1), leading to a non-zero offset in the average observed thermocline depth $\overline{h'}$. This bias

term is a function of both Φ_0 and U/c (Figure 2). The maximum value of the offset, or the bias in \bar{h}' , is $\sim 0.6A$ for $U/c \approx 1.7$, where A is the internal wave amplitude. For example, a moored sensor in a flow similar to of Figure 1b would observe a wave crest most of the time, followed by a brief downward excursion as the wave trough is swept past by the barotropic flow. A time average of measurements at this phase-offset is therefore biased towards the value at a wave crest; this is true for any observation window over an integer number of wave periods. Half a wavelength away (half a wavelength of the internal tide), the opposite bias is observed: the time-average is biased towards the wave trough value, to a minimum value of $\bar{h}' \approx -0.6A$, as shown in Figure 1f. For values of U/c increasing beyond 1.7, more wave crests are swept past the measurement platform in one tidal period, and therefore \bar{h}' tends to 0 as U/c tends to infinity.

This bias has consequences. If we assume that this is a 2-layer wave, then variation of \bar{h} with Φ_0 will appear as horizontal variations of the mean isopycnal depth, or, equivalently, as a horizontal density gradient. In a linear internal wave affected by the earth's rotation, the zonal velocity perturbation u' , vertical displacement h' , and pressure perturbation p' are $\pi/2$ radians out of phase with the meridional velocity perturbation v' . If \bar{h}' is at a maximum (as in Figure 1b), then $\bar{v}' = 0$ ($\pi/2$ radians offset), but \bar{u}' is also at a maximum. The depth-averaged flow remains zero for baroclinic motions, and there is therefore no net mass flux as a result of the advective interaction. However, in the upper and lower layers, $\bar{u}' \neq 0$ corresponds to time-averaged across-shore flow. At these locations, a mooring will observe time-averaged across-shelf flow in each layer. The direction of across-shelf flow reverses every half-wavelength. On the other hand, if $\bar{h}' = 0$, then $\bar{u}' = 0$, but \bar{v}' is at a maximum or minimum, corresponding to time-averaged along-shore flow. Assuming the phase offset Φ_0 is constant in time at a given location, as for locally-generated internal waves (Nash et al., 2012), the bias cannot be removed by extending the averaging time interval.

194 *c. Perturbations*

195 As we have shown, where the barotropic and baroclinic waves interact, the observed average
 196 may be biased. If perturbations, $\eta'(t)$ are calculated using the observed average, $\overline{\eta_0}$, as $\eta'(t) =$
 197 $\eta_0(t) - \overline{\eta_0}$, this bias is directly transferred to perturbation quantities. In the example in Figure 1b,
 198 the average observed value of the isotherm depth is $0.6A$; therefore, h' ranges from $-0.4A$ to $1.6A$.
 199 Similar conclusions hold for u' , v' , and p' .

200 In computing the baroclinic energy fluxes, we calculate $F = u'p'$. If the perturbation quantities
 201 are biased, the range of F increases. In the case of relatively weak advection ($U/c = 0.2$), the
 202 maximum value of the flux observed increases by only $\sim 15\%$, and at a given location the timing
 203 of baroclinic energy flux “pulses” is a function of the phase of the IW (Figure 3c). In contrast,
 204 when $U/c \approx 1.7$, η' ranges from -0.4 to 1.6 times its usual value. Therefore F ranges from 0.2 to
 205 2.56 times its ‘actual’ value. This serves to exaggerate non-linearity and intermittency in energy
 206 fluxes, which appear concentrated in a narrow time interval (Figure 3a). Furthermore, in this case,
 207 the peak baroclinic energy flux occurs at a particular phase of the barotropic tide (Figure 3b), while
 208 the phase of the IW contributes very little to the timing. The arrival time of a pulse of baroclinic
 209 energy is nearly uniform in x_r .

210 Tidally-averaged values ($\langle \rangle$) of F are also affected (Figure 4). As U/c increases from 0 , $\langle F \rangle$
 211 decreases, to a minimum of 0.5 times its value for the case of no advection. For $U/c > 2$ or
 212 3 (depending on Φ_0), $\langle F \rangle$ increases to a maximum of ~ 1.3 times its value for the case of no
 213 advection when $U/c \approx 3.3$. The magnitude of the decrease or increase is dependent on Φ_0 , and
 214 can be significant for relatively low values of U/c . For example, for $U/c \approx 0.6$, a decrease of
 215 up to 15% in the tidally-averaged fluxes is possible. It should be noted that this decrease is not

216 a result of filtering; rather, it is due to the bias in the observed average altering the values of the
217 perturbations used to calculate instantaneous fluxes.

218 *d. Spectra*

219 Another consequence of advection by oscillating barotropic flow is the alteration of the spectra
220 of the observed wave signal. In the case of no barotropic flow, the pure tone wave has energy only
221 at a single frequency. As noted above, as U/c increases, more wave crests are advected past the
222 observing platform and energy appears at higher frequencies (Figure 5), but remains concentrated
223 in harmonics of the fundamental frequency. This forces the observed signal to remain periodic
224 over one wave period while allowing the observed waveform to take many shapes. For the M_2
225 tide, as U/c increases, more energy appears at the M_4 , M_6 , M_8 , ... frequencies. The power spectra
226 depend mostly on U/c ; there is some spatial variability in the high-frequency content, but for
227 a given U/c only the highest frequency harmonics present are significantly affected by Φ_0 . The
228 amplitude of the spectral peak at each harmonic varies with U/c . In general, less energy is found in
229 lower harmonics as U/c increases, but the amplitude of a given harmonic and the relative energies
230 of any two harmonics are not simple functions of U/c (Figure 6).

231 The results in MacKinnon and Gregg (2003) are consistent with these findings. They examined
232 low-pass-filtered energy (M_2 and M_4) in vertical modes 1 through 5 and found that, although a
233 strong peak in M_2 energy was present in the lowest modes, it was absent in the higher modes.
234 For a given barotropic flow, higher-vertical mode waves have higher values of U/c in general, and
235 therefore will have less energy in lower harmonics. As the barotropic tidal amplitude increased,
236 MacKinnon and Gregg (2003) found changes in the partitioning of energy between vertical modes,
237 but no clear explanation for which modes had energy. This mirrors the results in Figure 6, which
238 show the oscillations of first and second harmonic amplitudes at large values of U/c .

239 The spectral energy contained in the observed signal, obtained by integrating the power spectra,
 240 is a function of both U/c and Φ_0 (Figure 7). For $U/c \sim 1.7$, the observed energy can range from
 241 0.5 to 1.5 times the true energy of the wave, depending on Φ_0 . As U/c increases, the sensitivity
 242 of the spectral energy to Φ_0 decreases; this is because Φ_0 affects only the amplitude of the few
 243 highest harmonics, so as energy is spread across more harmonics, Φ_0 dependence decreases. Peaks
 244 in observed energy occur π radians apart; the wavelength of the spectral energy is half that of the
 245 original wave. The spectral energy may correspond to kinetic or potential energy, depending
 246 on whether u' or h' is being measured. For a normal linear wave, these two quantities are $\pi/2$
 247 radians out of phase. The total observed energy (kinetic plus potential) is then constant, and any
 248 individual component (kinetic or potential energy) averaged over $1/2$ wavelength of the internal
 249 wave (neglecting k_0) will be constant. The periodic spatial variation in kinetic and potential energy
 250 resulting from the advection mechanism resembles a standing wave; indeed, it is possible that some
 251 features in shelf-seas with standing wave properties might be attributable to this interaction of the
 252 barotropic and baroclinic tides.

253 This spatial redistribution of kinetic and potential energy may help to explain the distribution
 254 of vertical mixing on the shelf. Dissipation measurements on the shelf contain many examples of
 255 “patchiness,” with turbulence concentrated over a small horizontal extent (e.g., Inall et al., 2000),
 256 whereas Palmer et al. (2015) found links between dissipation and the ratio of kinetic to potential
 257 energy. If an internal wave is most likely to break at one point in its phase (e.g., when vertical
 258 shear is a maximum), partial stalling of the propagating zone of maximum IT shear by opposing
 259 barotropic flow will tend to spatially concentrate the zone of maximum shear at one location (for
 260 example, at $x=0$), while at the same time spatially diluting the shear at another location ($x \approx \lambda/2$
 261 in this example, where λ is the wavelength of the IT). A similar mechanism may lead to spatial
 262 variability in bottom drag. The maximum flow speed over the seabed occurs where baroclinic ve-

263 locity in the lower layer is in phase with the barotropic flow. Barotropic advection of the IT leads
264 to spatial concentration of the higher bottom velocities, and may cause variability in bottom drag
265 with a spatial scale $\sim \lambda$. The advection mechanism also leads to near-bed flows with higher har-
266 monic frequencies; as these interact with sea floor topography, it may generate freely-propagating
267 waves at the higher harmonics, similar to the processes described in detail by Bell (1976).

268 4. Discussion

269 *a. Implications for baroclinic energy fluxes*

270 The aforementioned shifts in observed energy, both spatially and towards higher frequencies,
271 have important implications for estimates of baroclinic energy fluxes. The effects of advection
272 by the barotropic tide introduce a potential source of variability to estimates whose magnitude
273 depends in part on how data is collected and in part on how it is analyzed.

274 One approach to studying the internal tide is to use an array of moorings spanning the continental
275 shelf (e.g., Hopkins et al., 2014). As we have demonstrated, where U/c is large and in the absence
276 of actual energy dissipation, the observed kinetic and potential energy of the internal tide will vary
277 by up to $\pm 50\%$ over one half-wavelength of the internal tide. If the phase offset between a locally-
278 generated internal tide and the local barotropic tide is constant, then placement of a mooring may
279 bias observations of kinetic or potential energy by up to $\pm 50\%$ (depending on U/c). Although the
280 total energy (KE+PE) should remain constant, if moored instruments resolve one but not the other,
281 it may introduce a bias into wave field estimates.

282 There are many sources of variability in the ocean, and identifying the variability associated
283 with one particular process, such as the internal tide, is not easy. A standard analysis technique
284 is to filter data using a low-pass or band-pass filter to selectively retain the processes of interest.

285 Hopkins et al. (2014), for example, employed a band-pass filter to retain frequencies from 0.7 to
 286 1.5 M_2 . As we showed, however, the barotropic/baroclinic interaction shifts much of the observed
 287 energy into higher harmonics, even for reasonably small values of U/c . For any $U > 0$, there is
 288 some reduction in the energy present in the M_2 band. For $U/c \approx 0.5$, the observed energy at the
 289 M_2 frequency ranges from 90 to 97% of its “true” value, whereas for $U/c = 1$, it ranges from 65
 290 to 88% of the actual energy (Figure 8b). Based on the barotropic velocities reported in several
 291 studies, and estimating the phase speed of the mode-1 internal tide, we can estimate by how much
 292 a particular reported baroclinic energy flux may be underestimated.

293 Another approach to reconstructing the wave field is to employ a harmonic fit to a signal of
 294 known frequency. Since the frequency of our model wave is partially shifted, problems arise. A
 295 harmonic fit to the observed wave in Equation 2 produces amplitude and phase estimates that vary
 296 with U/c and Φ_0 (Figure 8a,c). As with the mean in Figure 2, this implies spatial variability in
 297 the amplitude and phase of a harmonic fit. If u' and p' are fit to a harmonic, baroclinic energy
 298 fluxes scale as $A_{fit}^2(\Phi)$, where A_{fit} is the amplitude of the harmonic fit. Variation of $A_{fit}^2(\Phi)$ with
 299 Φ_0 gives the appearance of horizontal divergence and convergence of energy flux. From such
 300 an observation, it would be natural to infer the existence of sinks (dissipation) or sources (local
 301 generation / tidal conversion) of energy. Figure 5 shows that the greatest energy flux divergence
 302 and convergence occurs when $U/c \approx 3.2$, where $F_{observed}$ ranges from 0.6 F to 1.3 F for an actual
 303 flux of F , with a second peak where $U/c \approx 1.4$, where $F_{observed}$ ranges from 0.5 F to 0.9 F . The
 304 important point is that there are no such processes in our model. The apparent dissipation is in this
 305 case only an artifact of a low-pass filter applied to advected internal waves.

306 The variation of harmonic fit *phase* with U/c is less important for baroclinic energy fluxes, but
 307 is relevant when considering the likelihood of local or remote generation of the internal tide, where
 308 ‘local’ implies constant phase offset relative to the barotropic tide and ‘remote’ is associated with

309 a phase offset that changes in time (e.g., Nash et al., 2012). In our model, the phase of a harmonic
 310 fit to the observed waveform is a function of the phase offset and the normalized barotropic flow
 311 speed U/c (Figure 8c). If we consider the spring-neap cycle of the tides as a slowly-modulated
 312 tide with a frequency close to M_2 , then it is clear that in the ocean as spring tide approaches, the
 313 amplitude of the barotropic current U increases, and therefore U/c increases. This alters the phase
 314 of the least-squares fit solution to the observed wave. Therefore, even if the locally-forced internal
 315 tide has a constant phase offset relative to the local barotropic tide, the phase of the M_2 harmonic
 316 fit to the observed internal tide will vary as U/c increases. Similarly, as stratification changes,
 317 whether due to seasonal heating and cooling or a one-off mixing event, the internal wave speed
 318 will change, altering U/c . Changes in stratification also change the wavelength of the internal tide,
 319 which may alter its phase offset relative to the local barotropic tide by modifying k_n in Equation 2.
 320 These effects may lead to the locally-generated internal tide being at least partially miscategorized
 321 as remotely-generated when separating locally- and remotely-generated tides on the basis of local
 322 coherence.

323 Spring-neap changes in U/c also affect the bias in observed baroclinic energy fluxes. With an
 324 averaging window long enough to capture changes in U/c , the observed bias will tend towards
 325 an average of the biases for the time-varying values of U/c . The variations in U/c included in
 326 a longer time-averaging window will not drive the bias towards zero. However, with longer time
 327 windows, other ocean processes that affect c or Φ_0 may influence the energy flux bias in ways that
 328 are difficult to generalize.

329 In light of our results, a reexamination of baroclinic flux estimates in shelf seas may be needed.
 330 There are two ways to calculate baroclinic energy flux (Kunze et al., 2002). The first decomposes
 331 motions into barotropic and a baroclinic components. The perturbation velocity (u') and pressure
 332 (p') associated with an internal tide are used to calculate the baroclinic energy flux, defined by

333 $F = \langle u' p' \rangle$, where $\langle \rangle$ denotes a time average over a tidal cycle (Nash et al., 2005). This de-
 334 composition can be done in such a way as to eliminate certain influences of the barotropic tide,
 335 such as isopycnal heave caused by the motion of the free-surface (Kelly et al., 2010). However,
 336 these techniques do not correct for effects of the wave-wave interaction, caused by lateral advec-
 337 tion of isopycnals by the barotropic tide.

338 The second approach measures the wave field, then calculates flux as $F = E c_g$, where E is the
 339 energy in the internal tide and c_g is the group velocity (See Inall et al., 2011 or Hopkins et al.,
 340 2014 for a more thorough discussion). It is clear that care must be taken in defining perturbation
 341 quantities, since spatial variability in the observed average is a consequence of advection by the
 342 barotropic tide. Inall et al. (2011) approached this problem with a towed undulator and found
 343 energy flux estimates of 940 W m^{-1} using $F = \langle u' p' \rangle$ and 1600 W m^{-1} using $F = E c_g$. By
 344 averaging spatially over one baroclinic wavelength, they avoided the spatial bias in energy fluxes.
 345 By limiting the amount of filtering done, energy shifted to higher frequency contributed to the
 346 total, rather than being filtered out. It is not entirely surprising, therefore, that their across-shelf
 347 baroclinic energy flux estimates are much larger than others in the same region ($O(100 \text{ W m}^{-1})$)
 348 (Green et al., 2008; Hopkins et al., 2014).

349 One concern with the second approach ($F = E c_g$) is the problem of partitioning energy between
 350 different vertical modes. The best estimate is of the form

$$F = \sum_{i=1}^{\infty} E_i c_i. \quad (9)$$

351 Higher mode waves dissipate over shorter horizontal length scales than low modes, so we expect
 352 most of the energy away from generation sites to be in the lowest modes. However, the mode-
 353 1 wave travels more quickly than other vertical modes, so assigning all baroclinic energy to the
 354 mode-1 wave is likely to overestimate the baroclinic energy.

Both approaches may introduce errors into baroclinic energy flux divergence calculations, and therefore into indirect estimates of energy dissipation. A tempting solution, reconstruction of the ‘unadvected’ internal wave field, might be feasible in theory, but has been difficult to implement in practice. As Pinkel (2008) explains: “[Doppler smearing] cannot, in general, be unscrambled, but the task is much easier if the spectrum consists of a few discrete lines.” This concurs with our experience: methods that accurately reconstruct synthetic advected waves fail on real ocean data.

b. Global applicability

Tidal energy conversion is directly proportional to U , and barotropic velocities generally increase as water depth decreases, whereas baroclinic wave speeds decrease. Therefore, we expect that the bias presented here will be present at most shallow internal tide generation sites and will be most pronounced in shelf seas with strong barotropic tides. To estimate the parameter U/c , we first calculated dynamical mode estimates of the mode-1 internal wave speed for the M_2 internal tide by solving the wave equation,

$$\frac{\partial^2 \eta}{\partial z^2} + \left(\frac{N^2 - \omega^2}{\omega^2 - f^2} \right) k^2 \eta = 0, \quad (10)$$

where N is the buoyancy frequency, ω is the wave frequency, f is the inertial frequency, and k is the horizontal wave number of the internal wave. Stratification profiles were derived from long-term average temperature and salinity profiles from the World Ocean Atlas (<https://www.nodc.noaa.gov/OC5/woa13/>) (Locarnini et al., 2013; Zweng et al., 2013). Then using tidal velocities from TPXO (<http://volkov.oce.orst.edu/tides/global.html>) (Egbert and Erofeeva, 2002), we estimate U/c for the first baroclinic mode. The results of the computation, shown in Figure 9, show that the ratio is greatest ($O(10)$) on the European Shelf. Elevated values are also evident east of Argentina, northwest of Australia, in the South China Sea, and on the New England

376 Shelf. Overall, these calculations indicate potential for $U/c > 1$ in $\sim 3.5\%$ of the ocean, or more
 377 than one third of the ocean shallower than 500 m. However, these measurements do not account
 378 for the relative directions of wave propagation and barotropic flow; internal tides propagating at
 379 angles to the semimajor axis of the barotropic tidal ellipses will have smaller values of U/c . Fur-
 380 thermore, seasonal variations in stratification will affect the values of c ; U/c is likely to be higher
 381 in winter than summer, especially in shelf seas where the annual cycle in stratification is large.
 382 Small values of U/c over the deep ocean mean that the abyssal ocean is unaffected by any bias.

383 Using the values of U/c in Figure 9, we calculate an ‘underestimation factor’ for baroclinic
 384 energy fluxes; this is the ‘worst-case’ estimate for how much a linear internal tide may be under-
 385 estimated using stationary sampling techniques and harmonic fits (the narrowest spectral filter),
 386 based on barotropic tidal advection of the baroclinic tide (see Figure 10 for details). We now apply
 387 this estimate to a baroclinic energy flux estimate in the Celtic Sea. At their mooring ST4, moored
 388 in ~ 160 m deep water on the continental shelf 40 km shoreward the shelf break, Hopkins et al.
 389 (2014) reported total average onshelf baroclinic fluxes of 93 W m^{-1} , and average semidiurnal on-
 390 shelf baroclinic energy fluxes of 28 W m^{-1} , a phase speed of 0.5-0.6 m/s for the mode-1 baroclinic
 391 tide, and maximum on-shelf barotropic currents of $\sim 0.4 \text{ m s}^{-1}$. Here U/c is ~ 0.7 -0.8. Referring
 392 to Figure 4, we estimate that the observed, unfiltered energy fluxes may represent as little as 75%
 393 of the total baroclinic energy fluxes present. Figure 8a indicates that the filtered amplitude of
 394 the observed internal tide ranges from 0.78 to 0.9 times its actual value. The amplitudes of the
 395 filtered baroclinic energy fluxes are calculated by squaring two filtered values, so the observed
 396 fluxes likely range from ~ 0.6 -0.8 times their actual value. In other words, the real values are esti-
 397 mated to be 25-67% higher. Computing empirical orthogonal functions (EOFs) of the across-shelf
 398 velocity, Hopkins et al. (2014) found that the mode-1 EOF accounted for 45% of the variance
 399 in the bandpassed across-shelf velocity fields, while the mode-2 EOF accounted for 11-16% of

400 the variance. With a phase speed of 0.3 m/s for the slower mode-2 baroclinic tide, U/c has a
 401 value of ~ 1.3 . This leads to unfiltered baroclinic energy flux estimates that capture only 55-85%
 402 of the total energy flux (as in Figure 4). With the higher mode wave, more baroclinic energy is
 403 shifted to higher harmonics that are filtered out before energy fluxes are calculated; the observed
 404 fluxes in the filtered data are only 0.2-0.6 times the “real” baroclinic energy fluxes, making the
 405 total values 67-400% larger. However, this and higher modes contain much less energy than the
 406 first mode. To evaluate the amount by which the filtered baroclinic energy fluxes underestimate
 407 the total, we need estimates of the modal distribution of energy fluxes. We assume the fraction of
 408 energy contained in a baroclinic mode is comparable to the fraction of variance explained by EOFs
 409 of baroclinic velocity in Hopkins et al (2014). For modes 1 and 2, we take these to be 45% and
 410 16%, respectively, and add a correction for each mode based on the value of U/c for that mode,
 411 as calculated above. The lower and upper bounds on the correction needed are as follows: *mode*
 412 *1*: (25 to 67% increase needed) \times 45% of baroclinic energy + *mode 2*: (67 to 400% increase) \times
 413 16% of baroclinic energy, all divided by (45% + 16%), the fraction of baroclinic energy in modes
 414 1 and 2. The result is that the filtered baroclinic energy fluxes should be between 36% and 150%
 415 larger than the original estimates. That is, the original estimates represent ~ 40 -73% of the energy
 416 flux. Rather than accounting for only 30% of the total baroclinic energy fluxes (28 W m^{-1} out of
 417 93 W m^{-1}), the semidiurnal internal tide is likely responsible for 40-75% of the total. Meanwhile,
 418 the original estimated total (unfiltered) baroclinic energy estimates likely captured 68-96% of the
 419 total baroclinic energy flux. The revised estimate of the total baroclinic energy flux ranges from
 420 97-136 W m^{-1} .

421 Studies in other shelf seas that have computed baroclinic energy fluxes using low-pass filters,
 422 bandpass filters, or harmonic fits have likely underestimated baroclinic energy fluxes in similar
 423 fashion. The information in Figure 4 and Figure 10 may be seen as first-order correction factors

that could be employed a posteriori to improve computations from any area. However, since tidal amplitude U changes over a spring-neap cycle and wave phase speed c changes with stratification, a more accurate estimate of the correction factor requires more specific values of U and c , rather than the values based on long-term averages. With a specific value of U/c , the upper and lower bounds on the underestimation can be inferred by reference to Figure 8a.

5. Conclusions

In this paper, we have explored a very simple model of a baroclinic tide advected by oscillating barotropic flow. Despite its simplicity, the model replicates many of the unusual features of the internal tide in shelf seas: unusual wave forms, high-frequency energy, and spatial and temporal variability in the phase and amplitude of the baroclinic tide. Our results suggest that advection of the internal tide by the barotropic tide biases observed average quantities, such as pressure and baroclinic velocity and hence also affect the perturbation quantities. As a result, baroclinic energy fluxes appear to be larger and more intermittent than they would in the absence of advection. These confounding factors make analysis of the internal tide more difficult, and expose a need for great care in analysing the internal tide in shelf seas. Neglecting this process where it is important can easily lead to a significant underestimate of the strength of baroclinic energy fluxes. On the other hand, although this barotropic/baroclinic interaction may lend the appearance of randomness to a well-ordered internal tide, it introduces the possibility that mechanisms governing temporal and spatial variability in internal tides may be less complicated than has been thought.

Our results suggest that correcting for the low bias in energy flux estimates in the Celtic Sea (Hopkins et al., 2014) may significantly increase estimates of total baroclinic energy fluxes, and will also increase the proportion of baroclinic energy fluxes attributed to the semidiurnal tide. In cases where data are strongly filtered, the increase can be a factor of 2 to 3. The adjustments

447 we have applied are fairly crude, however, and they do not close the gap in Celtic Sea baroclinic
448 energy fluxes. Accounting for and correcting the biases in various quantities, from, for example,
449 average thermocline displacement (Section 3.2) or baroclinic energy flux magnitude (Section 3.5)
450 will require some effort, and may change how we understand other shelf break processes. This
451 process is likely to be significant in many other shelf seas, but the global significance of the upward
452 adjustment we project in shelf seas baroclinic energy fluxes remains a subject of inquiry.

453 *Acknowledgments.* Funding was provided by NERC through FASTNet (grant NE/I030224/1).
454 The authors wish to acknowledge M. J. Lewis for useful discussions and three anonymous review-
455 ers for their helpful and insightful suggestions.

References

- Bell, T. J., 1976: The structure of internal wave spectra as determined from towed thermistor chain measurements. *J. Geophys. Res.*, **81**, 3709–3714, doi:10.1029/JC081i021p03709.
- Egbert, G., and S. Erofeeva, 2002: Efficient inverse modeling of barotropic ocean tides. *J. Atmos. Oceanic Technol.*, **19**, 183–204, doi:10.1175/1520-0426(2002)019<0183:EIMOBO>2.0.CO;2.
- Green, J., and J. Nycander, 2013: A comparison of tidal conversion parameterizations for tidal models. *J. Phys. Oceanogr.*, **43**, 104–119, doi:10.1175/JPO-D-12-023.1.
- Green, J., J. Simpson, S. Thorpe, and T. P. Rippeth, 2010: Observations of internal tidal waves in the isolated seasonally stratified region of the western Irish Sea. *Continental Shelf Res.*, **30**, 214–225, doi:10.1016/j.csr.2009.11.004.
- Green, J. A. M., J. H. Simpson, S. Legg, and M. R. Palmer, 2008: Internal waves, baroclinic energy fluxes, and mixing at the European shelf edge. *Continental Shelf Research*, **28**, 937–950, doi:10.1016/j.csr.2008.01.014.
- Holloway, G., 1983: A conjecture relating oceanic internal waves and small-scale processes. *Atmosphere-Ocean*, **21** (1), 107–122, doi:10.1080/07055900.1983.9649159.
- Hopkins, J. E., G. R. Stephenson, J. A. M. Green, and M. E. Inall, 2014: Storms modify baroclinic energy fluxes in a seasonally stratified shelf sea: inertial-tidal interaction. *J. Geophys. Res.*, **119**, 6863–6883, doi:10.1002/2014JC010011.
- Inall, M., D. Aleynik, T. Boyd, M. Palmer, and J. Sharples, 2011: Internal tide coherence and decay over a wide shelf sea. *Geophys. Res. Lett.*, **38** (L23607), doi:10.1029/2011GL049943.
- Inall, M. E., T. P. Rippeth, and T. J. Sherwin, 2000: Impact of nonlinear waves on the dissipation of internal tidal energy at a shelf break. *J. Geophys. Res.*, **105**, doi:8687-8705.

478 Kelly, S., J. Nash, and E. Kunze, 2010: Internal-tide energy over topography. *J. Geophys. Res.*,
 479 **115**, doi:10.1029/2009JC005618.

480 Kelly, S. M., N. L. Jones, J. D. Nash, and A. F. Waterhouse, 2013: The geography of semidiurnal
 481 mode-1 internal-tide energy loss. *Geophys. Res. Lett.*, **40**, 4689–4693, doi:10.1002/grl.50872.

482 Kunze, E., L. Rosenfeld, G. Carter, and M. Gregg, 2002: Internal waves in Monterey Submarine
 483 Canyon. *J. Phys. Oceanogr.*, **32**, 18901913.

484 Locarnini, R. A., and Coauthors, 2013: *World Ocean Atlas 2013, Volume 1: Temperature*, **Levitus,**
 485 **S. Ed., A. Mishonov Technical Ed. (NOAA Atlas NESDIS 73)**, 40 pp.

486 MacKinnon, J. A., and M. Gregg, 2003: Shear and baroclinic energy flux on the summer New
 487 England shelf. *J. Phys. Oceanogr.*, **33**, 1462–1475.

488 Melet, A., R. Hallberg, S. Legg, and K. Polzin, 2013: Sensitivity of the ocean state to the
 489 vertical distribution of internal-tide driven mixing. *J. Phys. Oceanogr.*, **43**, 602–615, doi:
 490 10.1175/JPO-D-12-055.1.

491 Nash, J., M. Alford, and E. Kunze, 2005: Estimating internal wave energy fluxes in the ocean. *J.*
 492 *Atmos. Oceanic Tech.*, **22**, 1551–1570, doi:10.1175/JTECH1784.1.

493 Nash, J., S. Kelly, E. Shroyer, J. Moum, and T. Duda, 2012: The unpredictable nature of internal
 494 tides on continental shelves. *J. Phys. Oceanogr.*, **42**, 1981–2000, doi:10.1175/JPO-D-12-028.1.

495 Osborne, A. R., T. L. Burch, and R. I. Scarlet, 1978: The influence of internal waves on deep-water
 496 drilling. *J. Petrol. Technol.*, **30**, 1497–1504.

497 Palmer, M., G. R. Stephenson, M. E. Inall, C. Balfour, A. Dusterhus, and J. A. M. Green, 2015:
 498 Turbulence and mixing by internal waves in the Celtic Sea determined from ocean glider mi-
 499 crostructure measurements. *J. Marine Systems*, **144**, 7–69.

500 Pinkel, R., 2008: Advection, phase distortion, and the frequency spectrum of finescale fields in
 501 the sea. *J. Phys. Oceanogr.*, **38**, 291–313, doi:10.1175/2007JPO3559.1.

502 Rippeth, T., and M. Inall, 2002: Observations of the internal tide and associated mixing across the
 503 Malin Shelf. *J. Geophys. Res.*, **107**, 11 980–11 990, doi:10.1029/2000JC000761.

504 Robins, P., and A. J. Elliott, 2009: The internal tide of the Gareloch, a Scottish fjord. *Estuarine,*
 505 *Coastal and Shelf Science*, **81**, 130–142.

506 Sharples, J., C. Moore, and E. Abraham, 2001: Internal tide dissipation, mixing, and vertical
 507 nitrate flux at the shelf edge of NE New Zealand. *J. Geophys. Res.*, **106**, 14 069–14 081.

508 Sharples, J., and Coauthors, 2007: Spring-neap modulation of internal tide mixing and vertical
 509 nitrate fluxes at a shelf edge in summer. *Limnol. Oceanogr.*, **52**, 1735–1747.

510 Shroyer, E., J. N. Moum, and J. Nash, 2011: Nonlinear internal waves over New Jersey’s conti-
 511 nental shelf. *J. Geophys. Res.*, **116** (C03022), doi:10.1029/2010JC006332.

512 Stephenson, G. R. J., J. E. Hopkins, J. A. M. Green, M. E. Inall, and M. R. Palmer, 2015: Wind-
 513 mixing by storms modifies baroclinic energy flux on the Celtic Sea shelf. *Geophys. Res. Lett.*,
 514 doi:10.1002/2014GL062627.

515 Vlasenko, V., N. Stashchuk, M. Inall, and J. E. Hopkins, 2014: Tidal energy conversion in a global
 516 hot spot: on the 3d dynamics of baroclinic tides at the Celtic Sea shelf break. *J. Geophys. Res.*,
 517 doi:10.1002/2013/C009708.

518 Wunsch, C., and R. Ferrari, 2004: Vertical mixing, energy, and the general circulation of the
 519 oceans. *Annu. Rev. Fluid Mech.*, **36**, 281–314, doi:10.1146/annurev.fluid.36.050802.122121.

520 Zweng, M., and Coauthors, 2013: *World Ocean Atlas 2013, Volume 2: Salinity*, Vol. 74. NOAA
 521 Atlas NESDIS, 39 pp. pp.

LIST OF FIGURES

- Fig. 1.** Observed waves (black) as in Equation 2 and least-squares sinusoidal fit to the observed wave (red) for $\frac{U}{c} = 1.7$ and phase offsets a) $\Phi_0 = 0$, b) $\Phi_0 = \frac{\pi}{3}$, c) $\Phi_0 = \frac{2\pi}{3}$, d) $\Phi_0 = \pi$, e) $\Phi_0 = \frac{4\pi}{3}$, and f) $\Phi_0 = \frac{5\pi}{3}$. Dashed lines indicate the mean value of the observed wave, averaged over an integer number of wave periods. 27
- Fig. 2.** The mean of the observed wave, as in Equation 2, as a function of Φ_0 and U/c 28
- Fig. 3.** Baroclinic energy flux, $F = u'p'$, where u' and p' are defined using Equation 2 with $A = 1$ and with the time-mean removed. a) Timeseries of F for $\frac{U}{c} = 0$, $\Phi_0 = \frac{\pi}{2}$ (green), $\frac{U}{c} = 1.7$, $\Phi_0 = \frac{\pi}{2}$ (red), and $\frac{U}{c} = 1.7$, $\Phi_0 = \pi$ (blue). Similar plots for a range of Φ_0 with b) $\frac{U}{c} = 1.7$, and c) $\frac{U}{c} = 0.2$ 29
- Fig. 4.** Tidally-averaged baroclinic energy flux $\langle F \rangle = \langle u'p' \rangle$, where u' and p' are defined using Equation 2 with $A = 1$ and with the time-mean removed. $\langle F \rangle$ is further normalized by the case where $U/c = 0$. Average fluxes vary with Φ_0 , but generally reach a minimum where $U/c \sim 2$ and a maximum where $U/c \sim 3$ 30
- Fig. 5.** Power spectra against frequency (y-axis) of the wave in Equation 2 as a function of $\frac{U}{c}$. Spectra have been averaged over $\Phi_0 \in [0, 2\pi)$. As $\frac{U}{c}$ increases, more energy is present at higher harmonics. 31
- Fig. 6.** Normalized spectral amplitude at harmonics of the M_2 tide for a freely propagating sine wave advected by sinusoidally oscillating flow of the same frequency, where the advective velocity, U , has been normalized by the speed of the wave, c 32
- Fig. 7.** The integral of the power spectra of the observed wave (as in Equation 2) over one wave period, normalized to 1 when $U = 0$. Observed signal power varies with $\frac{U}{c}$ and Φ_0 33
- Fig. 8.** a) The maximum (red) and minimum (blue) amplitude of a harmonic fit to the advected wave, as a function of U/c . The b) amplitude and c) phase of harmonic fits to the advected wave vary with U/c and Φ_0 . Contours are spaced 0.2 units apart. 34
- Fig. 9.** Global map of $\frac{U}{c}$ for (i) M_2 and (ii) K_1 tidal constituents. A mask (gray) has been applied over land surfaces and poleward of the critical latitude for each tidal frequency. 35
- Fig. 10.** Based on $\frac{U}{c}$ in Figure 9, the factor by which a harmonic fit (the most restrictive spectral filter) will underestimate an advected internal wave amplitude. For example, a value of 0.2 means that the amplitude of the harmonic fit is 20% the amplitude of the advected IW. 36

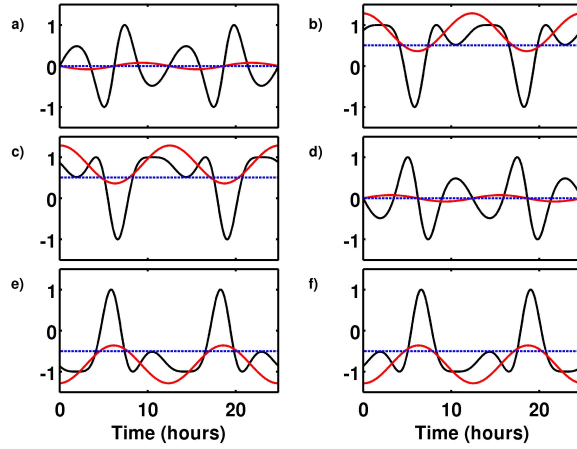


FIG. 1. Observed waves (black) as in Equation 2 and least-squares sinusoidal fit to the observed wave (red) for $\frac{U}{c} = 1.7$ and phase offsets a) $\Phi_0 = 0$, b) $\Phi_0 = \frac{\pi}{3}$, c) $\Phi_0 = \frac{2\pi}{3}$, d) $\Phi_0 = \pi$, e) $\Phi_0 = \frac{4\pi}{3}$, and f) $\Phi_0 = \frac{5\pi}{3}$. Dashed lines indicate the mean value of the observed wave, averaged over an integer number of wave periods.

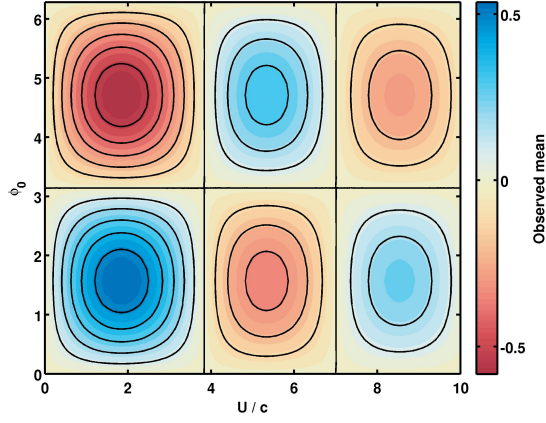


FIG. 2. The mean of the observed wave, as in Equation 2, as a function of Φ_0 and U/c .

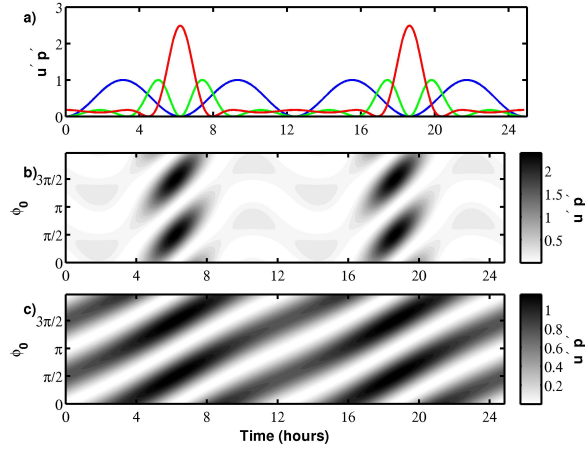
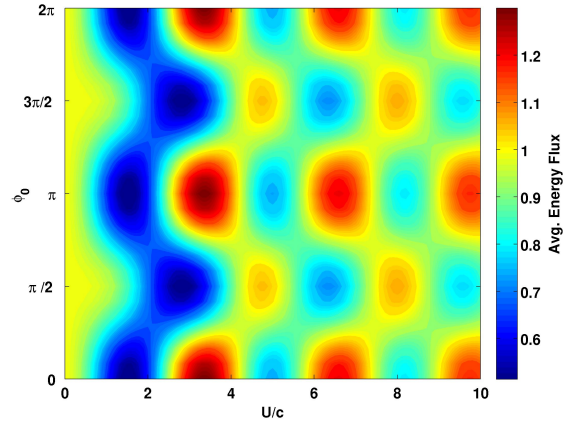


FIG. 3. Baroclinic energy flux, $F = u'p'$, where u' and p' are defined using Equation 2 with $A = 1$ and with the time-mean removed. a) Timeseries of F for $\frac{U}{c} = 0$, $\Phi_0 = \frac{\pi}{2}$ (green), $\frac{U}{c} = 1.7$, $\Phi_0 = \frac{\pi}{2}$ (red), and $\frac{U}{c} = 1.7$, $\Phi_0 = \pi$ (blue). Similar plots for a range of Φ_0 with b) $\frac{U}{c} = 1.7$, and c) $\frac{U}{c} = 0.2$.



558 FIG. 4. Tidally-averaged baroclinic energy flux $\langle F \rangle = \langle u' p' \rangle$, where u' and p' are defined using Equation 2
 559 with $A = 1$ and with the time-mean removed. $\langle F \rangle$ is further normalized by the case where $U/c = 0$. Average
 560 fluxes vary with Φ_0 , but generally reach a minimum where $U/c \sim 2$ and a maximum where $U/c \sim 3$.

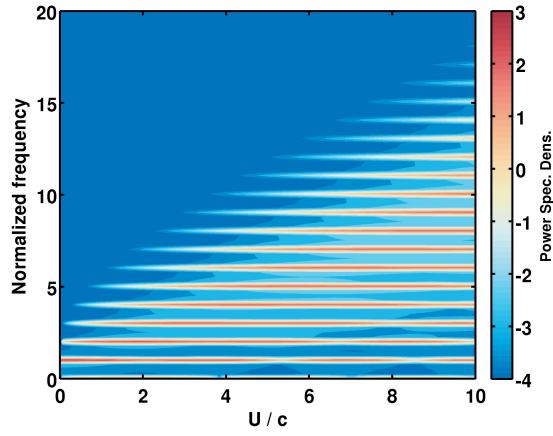
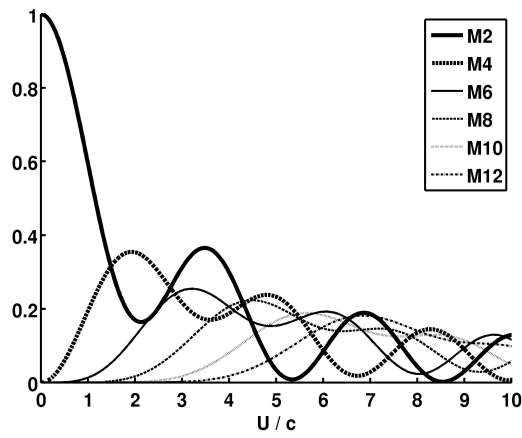


FIG. 5. Power spectra against frequency (y-axis) of the wave in Equation 2 as a function of $\frac{U}{c}$. Spectra have
 been averaged over $\Phi_0 \in [0, 2\pi)$. As $\frac{U}{c}$ increases, more energy is present at higher harmonics.



563 FIG. 6. Normalized spectral amplitude at harmonics of the M_2 tide for a freely propagating sine wave advected
 564 by sinusoidally oscillating flow of the same frequency, where the advective velocity, U , has been normalized by
 565 the speed of the wave, c .

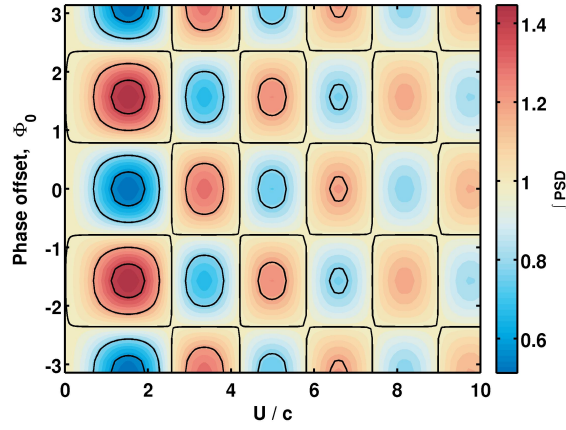


FIG. 7. The integral of the power spectra of the observed wave (as in Equation 2) over one wave period,
normalized to 1 when $U = 0$. Observed signal power varies with $\frac{U}{c}$ and Φ_0 .

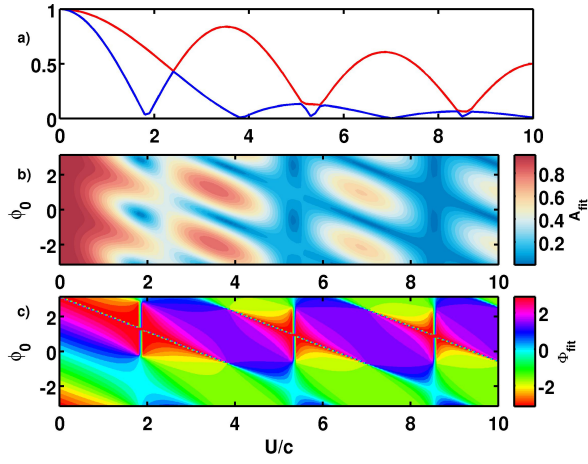


FIG. 8. a) The maximum (red) and minimum (blue) amplitude of a harmonic fit to the advected wave, as a function of U/c . The b) amplitude and c) phase of harmonic fits to the advected wave vary with U/c and Φ_0 . Contours are spaced 0.2 units apart.

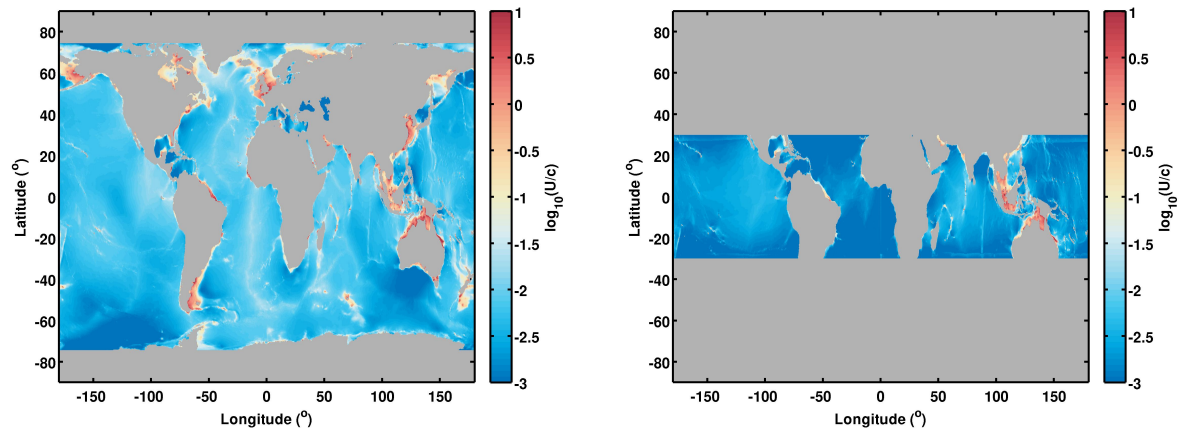


FIG. 9. Global map of $\frac{U}{c}$ for (i) M_2 and (ii) K_1 tidal constituents. A mask (gray) has been applied over land surfaces and poleward of the critical latitude for each tidal frequency.

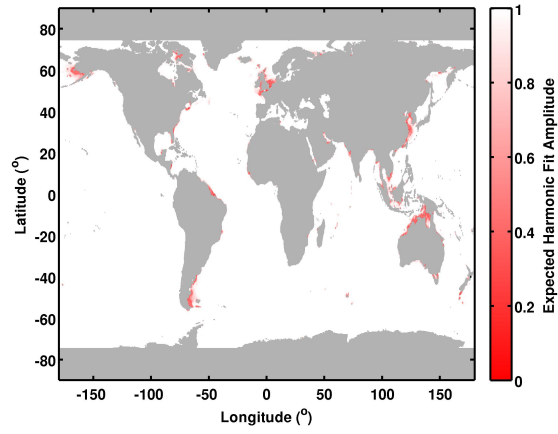


FIG. 10. Based on $\frac{U}{c}$ in Figure 9, the factor by which a harmonic fit (the most restrictive spectral filter) will underestimate an advected internal wave amplitude. For example, a value of 0.2 means that the amplitude of the harmonic fit is 20% the amplitude of the advected IW.